ARTICLES
https://doi.org/10.1038/s41928-019-0309-z
nature electronics

Three-dimensional imaging of integrated circuits with macro- to nanoscale zoom

Mirko Holler[1*], Michal Odstrcil[1], Manuel Guizar-Sicairos[1], Maxime Lebugle[1], Elisabeth Müller[1], Simone Finizio[1], Gemma Tinti[1], Christian David[1], Joshua Zusman[2], Walter Unglaub[2], Oliver Bunk[1], Jörg Raabe[1], A. F. J. Levi[2] and Gabriel Aeppli[1,3,4]

The imaging of integrated circuits across different length scales is required for failure analysis, design validation and quality control. At present, such inspection is accomplished using a hierarchy of different probes, from optical microscopy on the millimetre length scale to electron microscopy on the nanometre scale. Here we show that ptychographic X-ray laminography can provide non-destructive, three-dimensional views of integrated circuits, yielding both images of an entire chip volume and high-resolution images of arbitrarily chosen subregions. We demonstrate the approach using chips produced with 16 nm fin field-effect transistor technology, achieving a reconstruction resolution of 18.9 nm, and compare our results with photolithographic mask layout files and more conventional imaging approaches such as scanning electron microscopy. The technique should also be applicable to other branches of science and engineering where three-dimensional X-ray images of planar samples are required.

Non-destructive three-dimensional (3D) imaging over large volumes with nanoscale resolution is important for a variety of applications, from mapping the natural neural connectome[1,2] to inspecting silicon-based integrated circuits[3–6]. For integrated circuits, such inspection is required for failure analysis and security[7], and a hierarchy of probes are currently used to image at various length scales: from imaging the entire chip (millimetres) using optical microscopy to imaging individual features of the underlying transistors (nanometres) using transmission electron microscopy on thin slices prepared with a focused ion beam.

X-ray ptychography combines scanning X-ray microscopy and coherent diffractive imaging[8]. A sample is scanned in a coherent X-ray beam and the propagated diffraction patterns are recorded, in reciprocal space, for each scanning position. Iterative algorithms permit the reconstruction of projections of the sample, while the resolution is limited by neither the beam diameter nor the step size used in the scan, but is determined by the scattered X-rays that can be recorded with a sufficient signal-to-noise ratio as well as by the position accuracy and stability of the sample in the beam. Recently, we showed that ptychographic X-ray computed tomography (PXCT)—the combination of X-ray ptychography and computed tomography, which involves recording many projections of a sample at different sample orientations—can provide high-resolution 3D images of a complementary metal–oxide–semiconductor integrated circuit at 14.6 nm isotropic resolution[5].

In tomography, the axis of rotation is perpendicular to the propagation direction of the incident light. As a consequence, samples need to be specially created such that they can be accessed by the radiation from all projection angles from 0 to 180°. For integrated circuits, this requires the extraction from the chip of a close to cylindrical pillar, which, in our previous demonstration, was prepared by focused ion beam milling. While the subsequent tomography requires no slicing of the pillar, and is in that sense non-destructive, the extraction of the imaged pillar is a destructive and time-consuming task. Additionally, the region to be imaged must be selected before the pillar extraction, precluding zooming capability.

The preparation of cylindrical pillars from a region of interest could be avoided for tomography by mounting the sample with the axis of rotation parallel to the integrated circuit surface. However, this causes the effective thickness of the sample to increase in proportion with the incidence angle of the X-rays to the sample. The increased effective thickness increases the attenuation and thereby limits the angular range of the measurement, resulting in a missing wedge of data in reciprocal space (Fig. 1a). The situation may be improved by not having the axis of rotation perpendicular to the incoming beam. Imaging in this generalized geometry is called laminography[9–11], and hierarchical X-ray imaging has been demonstrated at low resolution[12]. The approach is well suited to flat samples, where the tilted rotation axis forbids access to momentum transfers within a cone—rather than wedge—of reciprocal space (Fig. 1b).

While it may seem, from the point of view of missing information, that the two geometries are similar, laminography has several important advantages. First, because the angle between the incoming X-ray beam and the surface is constant, the effective sample thickness to penetrate remains constant as well. Second, laminography simplifies preparation of planar samples to at most a uniform thinning of the substrate to manage attenuation, and provides flexibility to select the measurement position and to trade, for a given photon budget, resolution for measured volume. More specifically, zooming can be achieved by combining a variety of straightforward measures, including decreasing the sample raster steps and X-ray spot size, and increasing the counting times to capture more reliable high-angle scattering events.

Ptychographic X-ray laminography

In this Article, we report the 3D imaging of planar samples using ptychographic X-ray laminography (PyXL) (Fig. 1c). Ptychography scans are performed by moving the sample in a plane perpendicular

[1]Paul Scherrer Institut, Villigen PSI, Villigen, Switzerland. [2]Department of Electrical and Computer Engineering, University of Southern California, Los Angeles, CA, USA. [3]Department of Physics, ETH Zürich, Zürich, Switzerland. [4]Institut de Physique, EPFL, Lausanne, Switzerland. *e-mail: mirko.holler@psi.ch

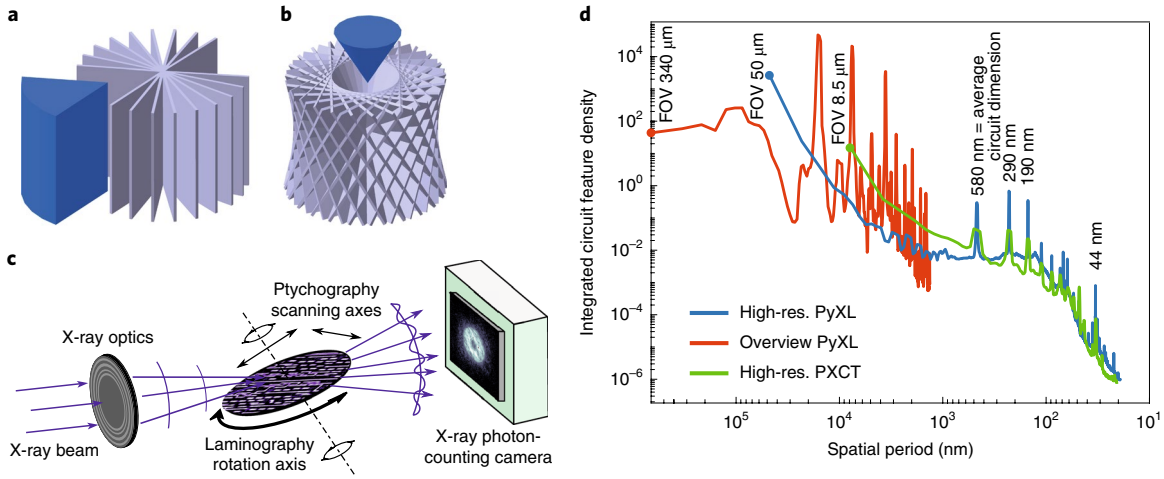

Fig. 1 | Imaging geometries. a,**b**, Illustration of the filling of Fourier space in tomography (missing wedge) for conventional tomography with $\theta = 90°$ (**a**) and in laminography (missing cone) for $\theta = 61°$ as in our instrument (**b**). **c**, Imaging geometry of PyXL. **d**, Density of chip features as a function of the in-plane component of the spatial period for PyXL in a high-resolution limited field of view (FOV) shown in blue and a low-resolution overview (with expanded FOV) modes shown in red, as well as for conventional PXCT depicted in green. The spikes are real and due to the multiscale design rules for the chip.

to the axis of rotation. Thereby, the sample is at a fixed distance from the beam conditioning optics, allowing the use of conventional ptychography algorithms. We developed and built an instrument dedicated to PyXL in which the sample position is measured with respect to beam defining optics via differential laser interferometry[13], similar to the previously described tomography instruments[14,15]. The interferometer positions are used to operate a piezo scanner in a closed loop, which in turn is mounted on an axis of rotation for laminography. The diffracted X-rays propagate to a pixelated photon-counting detector in the far field through a helium-filled flight tube. Choosing the laminography angle θ requires a balance between minimizing the missing information cone and providing sufficient transmission through the sample, and in our case it is set to $\theta = 61°$. While the scan range of the piezoelectric stage is only $100 \times 100\,\mu m^2$, the axis of rotation is mounted on two linear stages, allowing stitching of several such scan regions and thereby sampling of any selected region of interest in the sample. The maximum sample area that can be imaged in the instrument is $12 \times 12\,mm^2$, beyond the die size of many integrated circuits in daily use.

We also address the image reconstruction challenge created by the missing cone of information in reciprocal space (Fig. 1b), which is inherent to the laminography geometry (Fig. 1c). When standard reconstruction methods such as filtered backprojection[16,17] are used, the missing cone remains empty, resulting in unphysical artefacts (Supplementary Fig. 1b). Instead, we use an iterative approach that enforces consistency in the Fourier (reciprocal space) domain between the reconstruction and the measured data and two additional priors in real space. The first prior is based on knowledge of the sample composition and limits the electron density of the sample material to a range between that of SiO_2 and Cu. The second prior uses the assumption of a compact shape of the copper interconnects by driving the solution towards a minimal local total variation[18]. Iterative enforcement of these constraints in combination with a pyramidal multiscale approach improves the 3D reconstruction considerably (Supplementary Fig. 1c). Note that the refined reconstruction is still fully consistent with all measured data. In the future, for a more self-contained approach, it may be possible to learn the density constraints from the measured data and, in this way, eliminate introduction of ad hoc priors.

Imaging of integrated circuits and method comparison

We demonstrate PyXL by imaging an integrated circuit and comparing the result with its Graphic Database System (GDS-II) photolithographic mask layout files and also with the more conventional imaging approaches of PXCT and scanning electron microscopy (SEM).

The samples used are several identical chips produced in 16 nm fin field-effect transistor technology for general purpose logic. The transistors are on a single-crystal silicon substrate and are electrically connected by more than a dozen metal interconnect layers that are embedded in SiO_2 dielectric. The convention is to label the metal layers in sequence, M0, M1, M2 and so on, with M0 closest to the transistor layer. The total thickness of all of the layers and interconnect vias is about $T = 4\,\mu m$. We define T as the active layer thickness. For PXCT, a cylindrical pillar of 10 µm diameter was prepared using a focused gallium ion beam in a scanning electron microscope and measured as for previous studies[5]. In total, 914 projections were acquired and we obtained an isotropic resolution of 16.5 nm, determined using Fourier shell correlation[19]. Further details are given in Methods.

For laminography, we mechanically polished an entire chip of $2.5 \times 2.5\,mm^2$ to a substrate thickness of about 20 µm to obtain sufficient transmission of approximately 25% for 6.2 keV X-rays. Supplementary Fig. 2 shows a visible light micrograph of the chip surface with the circular flip-chip solder bonding areas clearly seen. These have a pitch of 170 µm. First, to obtain an overview image covering the region of interest and also demonstrating the stitching capabilities of the instrument, a near-field ptychography scan[20] was performed with a 50 µm X-ray beam diameter. A total area of $300 \times 300\,\mu m^2$ was covered by stitching ptychographic measurements from 25 subscans, each containing a region of $70 \times 70\,\mu m^2$. In this overview mode the resolution obtained was 0.5 µm, limited by the reconstruction pixel size, which is given by the beam numerical aperture and the detector pixel size. Further details can be found in Methods. A low-resolution 3D PyXL overview image was reconstructed using 300 such projections.

For the high-resolution PyXL measurement a 40 µm diameter region was virtually selected in the overview dataset, also containing the region measured via PXCT in the first sample. The X-ray beam size was reduced to 4 µm, and $N = 2{,}872$ projections were recorded in an angular range from 0 to 360°. With a chip $T = 4\,\mu m$ this angular

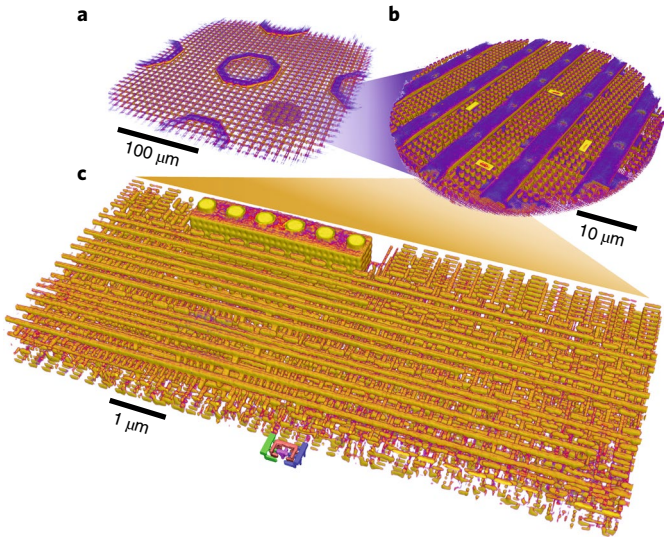

Fig. 2 | 3D renderings at different zoom levels covering a length-scale range from a 300 µm overview to nanometric device structures. a, The near-field ptychography results, giving a low-resolution overview measurement covering a chip area of 300 × 300 µm² with 500 nm resolution. **a**,**b**, The area measured via PyXL at high resolution is highlighted in **a** and shown in an isolated view in **b**. **c**, Further zooming to the active structures, revealing fine details down to the reconstruction resolution of 18.9 nm. All device layers and connections between them are resolved. The front edge of the volume rendering is cropped to expose the manually segmented inverter logic presented in Fig. 3a in detail.

sampling would allow a resolution no better than 7.6 nm at a laminography angle of 61° according to the laminography sampling equation, $\Delta r = \pi \frac{T}{N} \tan\theta$, derived in Methods. This is lower than the limit of 12 nm posed by the depth of field[21].

Figure 1d shows the densities of chip features as a function of their spatial period, collected using PXCT and PyXL. This was computed in the two lowest layers, referred to as M0 and M1, by means of a normalized power spectral density of the reconstructed electron density. The sharp peaks are real and due to the chip's hierarchical design rules, which impose quasiperiodic features for periods varying by several orders of magnitude. Naturally the peaks are sharper (and more intense) for the larger fields of view possible for PyXL because the sampled volumes are larger, implying better definition of quasiperiodic structures, and hence leading to two additional decades of useful spatial information in the form of visible maxima for PyXL compared with PXCT. The large advance represented by PyXL is thus very clear: with a single instrument we are now able to efficiently visualize the multiscale 'connectome' for an integrated circuit from the millimetre to 10 nm scales. Figure 2 shows 3D renderings of the reconstructed volumes measured via PyXL at various length scales down to the device level. The rendering was created by applying a threshold to the data, and it covers five orders of magnitude in length scales, revealing device details as well as features at the 100 µm scale of the overview. Supplementary Video 1 shows such zooming capabilities in an animation, and Supplementary Fig. 3 shows slices of the raw reconstructions of the two lowest metal layers of the chip, M0 and M1, unaltered by thresholding and segmentation.

For both PXCT and PyXL, the resolution is sufficient to identify all interconnections down to the individual transistors, even though the laminography resolution volume is anisotropic because of the missing cone of information (Fig. 1b). For tomography, Fourier shell correlation[19] is an established method for estimating the resolution. In the case of laminography it remains a valid estimator as long as it is only computed in the valid Fourier regions and not in the missing cone. Such analysis will provide a measure of the obtained average resolution in the Fourier directions where data are available, meaning that the resolution will worsen along the direction of the rotation axis. For the present measurement a resolution of 18.9 nm was estimated, and thus we expect that imaging of even more advanced technology is possible today. As an example, on passing from 16 nm to 7 nm technology, the minimum metal pitch in technology decreases from 64 nm to 40 nm, still considerably larger than our present resolution. We did not procure a physical chip paired with a design file at the 7 nm node, so for this first demonstration of PyXL 16 nm technology was imaged instead.

An interesting question, especially in the context of security, is whether and where certain electronic building blocks of a particular type exist within a manufactured integrated circuit. As an example, an inverter circuit was chosen, and to automate the search we used the known GDS-II model to render a corresponding 3D volume with a voxel size identical to the PyXL reconstruction, shown in Fig. 3a next to Fig. 3b, which is the underlying electrical circuit schematic. We then calculated the expected reconstruction volume by removing its Fourier components within the missing cone in reciprocal space. The coordinates of the inverter pattern, corresponding to the GDS-II model, were then found in the measured dataset at low computational cost using 3D cross-correlation. We manually segmented the single inverter found in the PyXL dataset and rendered it as the interpolated surface view shown in Figs. 2c and 3c. The expected structure rendered from the GDS-II file in Fig. 3a shows also individual fins that cannot be identified in the measured data. Supplementary Video 2 shows the slices of the inverter (Fig. 3) with the measured image and GDS-II model side by side. The automatic search of circuitry from the GDS-II in the measured data can be extended to larger blocks and thereby provides a fast method to verify that chip design and manufacture match and no undesired functionality (for example a backdoor into a processor or memory) has been introduced.

PyXL represents the only non-destructive method for nanometre-resolution analysis of integrated circuits. Commonly used methods for nanometre-scale imaging of integrated circuits, such as mechanical delayering and imaging by SEM, are destructive. As a consequence not only can the sample not be re-examined after the imaging process, but also the images obtained may not even reflect the previous state of the integrated circuit because of sample modification during the preparation steps. The non-destructive nature of PyXL therefore may be especially useful when investigating integrated circuit failure, as caused for example by electrostatic discharge. Nonetheless, it remains important to compare the imaging quality of PyXL with established techniques, so one of our samples was mechanically polished to expose the second-lowest metal layer, referred to as M1, and imaged using SEM with an electron energy of 5 keV. Figure 4 shows the direct comparison of the results obtained by SEM, PXCT and PyXL. For completeness, the corresponding (simplified) photolithographic mask layout of the same layer is also shown. Clearly, SEM provides highest image quality within a given two-dimensional plane. However, it is a destructive multistep technique and artefacts may occur due to the unavoidable and imperfect mechanical removal of material to expose the sample plane of interest. For example, the failure to mechanically delayer to the precise location of the M1 metal layer is apparent because bright spots in the image correspond to the locations of vias connecting M1 to the third-lowest layer M2.

PyXL is well suited for imaging integrated circuits, and in-plane features provided by PyXL are clearer and contain fewer artefacts compared with PXCT. This is most probably due to a combination of (1) a limited depth of field[21], which is less limiting for PyXL because in this measurement geometry the effective thickness along the X-ray propagation is slightly smaller,

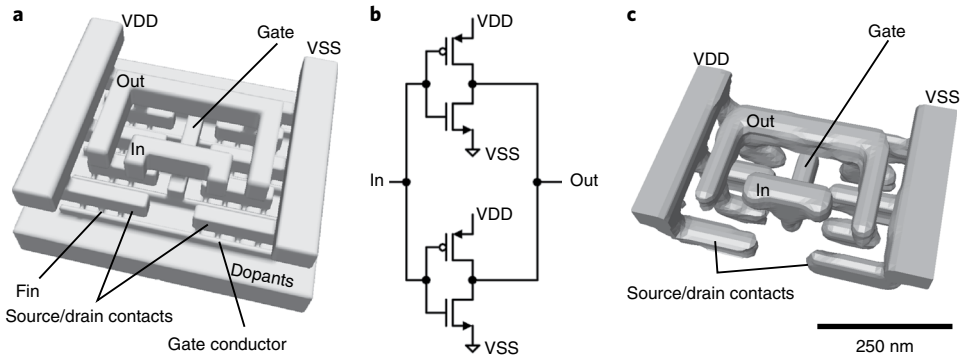

Fig. 3 | 3D rendering and circuit diagram of an inverter. VDD and VSS are supply voltages of the device, 'In' labels the input and 'Out' the output. The associated metal layer is M1. **a**, The expected device structure generated from the GDS-II model is rendered. Here also details not resolved in the measurement are shown, such as the fins and gate conductors. **b**, The electronic circuit representation. **c**, The structure identified in the volume of the high-resolution PyXL measurement. It has been manually segmented and is shown as an interpolated surface rendering. The 250 nm scale bar is valid for **a** and **c**.

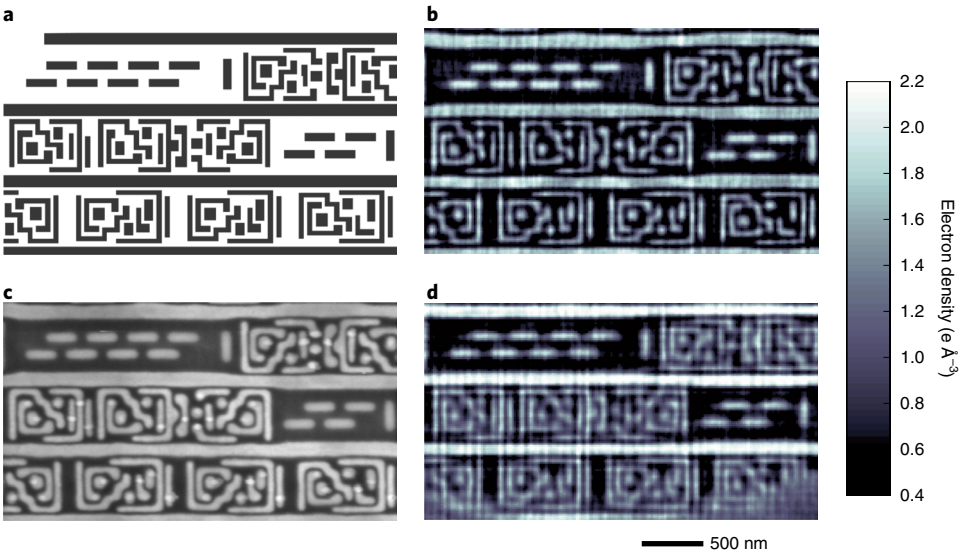

Fig. 4 | Comparison of different imaging techniques applied to different samples of the same chip area, showing the second-lowest metal layer M1. **a**–**d**, Design layout (simplified) (**a**) and virtual slices obtained from PyXL after missing cone refinement (**b**), SEM (**c**) and PXCT (**d**). The grey-scale bar shown applies to the quantitative X-ray images in **b** and **d**, and the bright lines correspond to connections manufactured from Cu surrounded by SiO_2. The region of interest shown here was close to the edge of the extracted pillar for PXCT in **d**, which explains the missing features in the lower right corner.

and (2) the improved nanostructural stability of a wafer (PyXL) relative to that of an isolated pillar (PXCT) when strongly irradiated by X-rays[5]. The streaking artefacts for PXCT are caused by the long straight metal line features, which dominate when imaged parallel to the direction of X-ray propagation, resulting in phase jumps larger than 2π, and thereby causing artefacts in the reconstruction. For PyXL the X-rays are not parallel to the direction of these structures, making PyXL less prone to these artefacts. However, for PyXL the resolution is anisotropic, which results in artefacts of a different type in the direction of the missing cone, that is, perpendicular to the individual layers. For comparison of PXCT and PyXL Supplementary Fig. 1 shows two slices perpendicular to the layers of the chip. Here the structures appear less sharp in the vertical direction for PyXL.

Conclusions

We have reported PyXL, a technique that can image extended flat samples in three dimensions with nanoscale resolution and minimal sample preparation. Low-resolution, fast 3D overview scans can be performed without any modification in the setup, and the region of interest for high-resolution 3D imaging can be freely chosen on the basis of the overview. For our test chip, such a low-resolution (500 nm) scan over an area of $300 \times 300\,\mu m^2$, yielding an image with 2.3×10^7 voxels (cubic with side length 500 nm), was collected in 30 h; a high-resolution (18.9 nm) zoom over a subarea 40 µm in diameter, which produced $3{,}800 \times 3{,}800 \times 600$ voxels with dimensions $13 \times 13 \times 13\,nm^3$, required 60 h. The latter chip area was 16 times larger than that which we could image using conventional PXCT at 16.5 nm resolution in 23 h, demonstrating that for the layered integrated circuit in the present case our laminography measurement, where (unlike PXCT) the more feature-rich planar structures are projected onto both dimensions of the area detector, is about six times more efficient for generating significant information at high resolution. This includes the images themselves and also the possibility of finding functional features, such as the presence and location of a single inverter circuit.

Currently the imaging rate, volume and resolution are limited by the available coherent X-ray flux. As outlined previously[5], we expect marked improvements in the near future. Such improvements follow the transition from third- to fourth-generation synchrotron sources, as pioneered by the Swedish MAXLAB[22], from which we expect an increase by two orders of magnitude in brilliance, and the construction of megahertz-repetition-rate X-ray free-electron lasers including LCLS II at SLAC in California. In addition, the spectral bandwidth used in our experiment, which is determined by a Si(111) monochromator, could be relaxed by an order of magnitude by using multilayer mirrors[23]. Furthermore, our Fresnel zone plates (FZPs) provide limited efficiency compared with, for example, Kirkpatrick–Baez mirror systems[24], which could provide an additional order of magnitude improvement. The total increase in coherent flux could thus reach 10^4, which could be combined with further advances from using an evacuated flight tube and in-vacuum detection, implying even greater efficiency for PyXL.

The scaling laws[25] for ptychographic imaging would thus allow approaching a resolution of 2 nm with the same measurement time as for the current experiment, or inspection of an entire $0.3\times0.3\,mm^2$ integrated circuit at 50 nm resolution in 3 h. Beyond higher flux, reaching such imaging speed and/or resolution will require additional developments for faster and more accurate sample scanning, improved X-ray probe stability and a careful management of radiation damage. In that context, the latest mechanical and electronic hardware can already improve the imaging rate by a further decrease in imaging overhead[26]. Additionally, laminography reconstruction algorithms could benefit from the sparse, laminar structure of ICs, as well as knowledge of other priors from design files and fabrication practice, leading to measurements requiring fewer projections. In the area of ptychographic reconstruction, significant development is necessary and ongoing[21,27,28] to reliably overcome the depth of field limitation on resolution, which is 12 nm for the present sample and photon energy, to approach 2 nm. Radiation damage may pose another limit to achievable resolution, although as mentioned above we observe significantly better sample stability for laminography compared with tomography requiring isolated pillars. Small deformations that may occur during a measurement at higher dose can also be dealt with in the reconstruction step[29].

Beyond the measurement of integrated circuits for failure analysis, design validation and quality control, our imaging method is applicable to any scientific, medical or engineering problem where the samples are planar. In reflection mode, its application could become a practical 3D imaging technique for unthinned samples, further opening up low-energy (soft) X-ray investigations in areas from biomedicine to magnetic devices.

Methods

X-ray measurements. All X-ray measurements were carried out at the cSAXS beamline of the Swiss Light Source at the Paul Scherrer Institut, Switzerland. The photon energy of 6.2 keV with a spectral bandwidth of 2×10^{-4} was selected using a double-crystal silicon monochromator. For both PXCT and PyXL a 170 µm diameter gold FZP with a 60 nm outermost zone width was used in combination with a 50 µm central stop and 30 µm order sorting aperture to define a 3–4 µm diameter illumination on the sample. The FZPs were manufactured in the Laboratory for Micro and Nanotechnology, Paul Scherrer Institut, Switzerland, on the basis of a nanofabrication process published elsewhere[30].

The PXCT data were measured using the flexible tOMography NanoImaging instrument (flOMNI)[13,14,31] with a PILATUS photon-counting detector[32] with 172 µm pixel size positioned at a distance of 7,386 mm from the sample, using 600×600 pixels for the reconstruction, resulting in a reconstructed pixel size of 14.3 nm. 914 projections were acquired, each having an FOV of $18\times9\,\mu m^2$. The 328 scan positions of each projection followed a Fermat spiral trajectory[33] and had an average spacing of 0.7 µm and 0.1 s exposure time. The sample was positioned downstream from the focal point of the FZP, where the beam diameter was 3 µm. The measurement time per projection was 90 s. The deposited X-ray dose into the copper interconnects for the whole tomogram was estimated to be 55 MGy. The tomogram was reconstructed to a voxel size of 14.3 nm in a way akin to the procedure used in ref. [5]: the complex-valued projections were reconstructed using 1,200 iterations of the difference map solver[34] followed by 300 iterations of the maximum-likelihood refinement[35]. For tomography, the phase of the reconstructed projections was used after postprocessing alignment and removal of constant and linear phase components[36]. A modified filtered backprojection was used after aligning the projections using a tomographic consistency approach[37].

PyXL laminography measurements were carried out using the laminography nanoimaging instrument. For the high-resolution scan, a circular FOV of 40 µm diameter was virtually defined in the sample surface plane such that the imaged volume is about a factor of 16 larger than in the case of PXCT. Because the device geometry and the position measurement are perpendicular to the X-ray beam propagation direction, this circular FOV in the sample plane results in an elliptical FOV of about $50\times26\,\mu m^2$ in the position-measurement plane, which is perpendicular to the X-ray beam propagation direction, as shown in Supplementary Fig. 4. The 485 scan points in that region of interest followed the Fermat spiral trajectory[33] and had an average spacing of 0.7 µm in the position-measurement plane and 0.1 s exposure time. The sample was positioned downstream from the focal position, where the beam diameter was 4 µm. A total of 2,872 projections were recorded at angles equally spaced in the range of 0–360°. The time to record a single projection was 67 s and the overhead between two projections for rotating and following the region of interest was 9 s. The resulting X-ray dose experienced by the copper interconnects for the whole laminogram is estimated at 76 MGy. The complex-valued projections were reconstructed using 300 iterations of the difference map solver[34] followed by 200 iterations of the maximum-likelihood refinement[35] using 480×480 pixels of the Eiger photon-counting detector[38] with 75 µm pixel size positioned at a distance of 2,345 mm after the sample, resulting in a pixel size of 13.0 nm. Supplementary Fig. 4b shows a reconstructed projection. The phase projections were unwrapped and aligned using a new in-house-developed iterative algorithm based on 3D consistency and a pyramidal approach in which the reconstruction and alignment are refined starting from low to progressively increased resolution. The initial 3D volume reconstruction was provided by the filtered backprojection method with the filtering kernel multiplied by $\sin(\theta)$ to account for the laminography geometry[39]. Given sufficient angular sampling, the filtered backprojection method provides an optimal reconstruction, X_{FBP}, up to the missing cone region in the Fourier space. The values inside the missing cone were estimated by an iterative scheme in which the 3D volume was Fourier transformed back and forth between object and reciprocal space. In reciprocal space, consistency with the known Fourier components, which were obtained in the previous step, was enforced outside the missing cone. Additional prior knowledge about the sample, as discussed in the main text, was enforced in object space. This process can be described as an alternating projection method between two constraints, Π_o, which applies object space priors, and Π_F, which enforces consistency in Fourier space:

$$\Pi_o : X \rightarrow X_o = \max\{X_{min}, \min[X_{max}, X - \mu\nabla_X O_{TV}]\}$$

$$\Pi_F : X \rightarrow X_F = X_{FBP} + \mathcal{F}^{-1}[S_c\mathcal{F}(X - X_{FBP})]$$

where X denotes the refined electron density and X_{min}, X_{max} are limits of the maximum and minimum electron density values given by the known composition of the sample. In object space, the refined reconstruction X is additionally updated by a gradient of a regularization functional $\nabla_X O_{TV}$, in our case the total variation[18], with updated step size μ. Finally, in reciprocal space, that is after the Fourier transform $\mathcal{F}$, S_c denotes the missing cone region defined as

$$S_c(k_x, k_y, k_z) = \begin{cases} 0, & \text{if } k_x^2 + k_y^2 < k_z^2 \tan^2\theta \\ 1, & \text{else} \end{cases}$$

where k_z is the reciprocal space coordinate parallel to the rotation axis and k_x, k_y are the perpendicular direction coordinates. An alternative approach would be an iterative use of the Radon transform to enforce consistency with the measured projections[40]; however, the large volume of our reconstruction makes the Fourier-transform-based approach significantly faster. Additionally, to further accelerate the convergence and reduce the computational cost, we have used a pyramidal approach, in which the missing cone refinement starts from the lowest spatial frequencies and progressively includes a larger fraction of the Fourier space while continuously enforcing the priors in the object space.

The reconstructed voxel size was 13.0 nm and the volume covers $3{,}800\times3{,}800\times600$ elements. The resolution was estimated to be 18.9 nm using an intersection of the Fourier shell correlation curve and the one-bit threshold[19]. The missing cone was excluded from the Fourier shell correlation calculation. The computation of the two-dimensional ptychographic reconstructions of this high-resolution laminography dataset required 4.7 h using eight nodes equipped with 28-core CPU Intel Xeon E5-2690 v4 processors. The computation time for the 3D laminography reconstruction using the filtered backprojection method was 40 min using a single Nvidia P100 GPU. The total time for the 3D reconstruction including data loading, alignment of the projections, filtered backprojection reconstruction and filling of the missing cone was 4 h.

The near-field ptychographic laminography data shown in Fig. 2a and Supplementary Fig. 5b were measured using a setup identical to that used for the

far-field ptychographic laminography. The only required change, of the beam diameter to 50 µm, was achieved by changing to an FZP with a diameter of 120 µm instead of 170 µm, which we manufactured on the same membrane such that no manual interaction with the setup was required. The distance from the sample to the detector of 2,345 mm and the Eiger detector pixel size of 75 µm resulted in a projected pixel size on the image plane of 495 nm, which was found to be the limit for the resolution. For this coarse laminogram, an FOV of $300 \times 300\,\mu m^2$ was measured with the Fermat spiral trajectory[33] implemented with an average step size of 10 µm. To cover the FOV for each projection, 25 patches, each $70 \times 70\,\mu m^2$ in size, have been measured via stitching and reconstructed together. 300 projections were acquired, aligned using the same algorithms as for the high-resolution PyXL reconstruction. The time to measure each projection patch was 14 s, including the overhead for moving to the next stitching patch with the coarse stage. Supplementary Table 1 gives a brief overview and comparison of the three X-ray measurements performed.

Angular sampling requirements for laminography. Similar to the Crowther criterion[41] for conventional tomography, for laminography the angular step should be sufficiently small for adequate sampling of the object's 3D Fourier transform. Supplementary Fig. 6a shows schematically the experimental realization with a fixed source under a parallel beam, and Supplementary Fig. 6b the equivalent representation with a fixed object and a source rotating around it. Invoking the Fourier projection-slice theorem we know that each laminography projection contains information about a thin slice in the Fourier domain going through the origin and with normal parallel to the beam propagation direction, as shown schematically in Supplementary Fig. 6c, where the Fourier domain radius is inversely proportional to the real-space projection resolution Δr. The sampling requirement for laminography is that these Fourier slices are taken close enough to each other to capture all details in Fourier space along the direction parallel to the rotation axis, as illustrated in the inset of Supplementary Fig. 6c. Assuming that the sample thickness along the axis of rotation T is much smaller than the other sample dimensions, from this criterion it readily follows that

$$\tan\theta = \frac{2\,\Delta r}{T\,\Delta\varphi}$$

where θ is the angle between the beam propagation direction and the axis of rotation, and $\Delta\varphi$ is the laminography angular step. Considering that for laminography the rotation is from 0 to 2π, the required N is given by

$$N = \frac{2\pi}{\Delta\varphi} = \pi\frac{T}{\Delta r}\tan\theta$$

For someone familiar with the Crowther tomography criterion[41], it may seem counterintuitive that the equation is completely independent of the FOV; however, this is actually sensible and expected. The key difference from conventional tomography, which depends on the horizontal sample diameter, arises from the inclination of the measured Fourier slices, as shown in Fig. 1b. Because of this inclination we have guaranteed adequate sampling in the plane perpendicular to the rotation axis. Another way to intuitively understand that this equation should be independent of the FOV is to consider that once we measure laminography projections we could always artificially reduce this FOV in postprocessing by cropping them, and of course we would not expect that by cropping the FOV our angular sampling would be relaxed.

Finally, the $\tan\theta$ factor shows that the most relaxed angular requirements are for small values of θ; however, this is only because for small values of θ the 3D information in the reconstruction is heavily reduced, both because the missing cone information grows significantly and because the resolution in the direction of the axis of rotation Δz is worsened,

$$\Delta z = \frac{\Delta r}{\sin\theta}$$

Through numerical simulations we have observed that $\theta > \pi/4$ provides a significant reduction of missing cone artefacts, and that best image quality is obtained for larger values of θ, even if somewhat angularly undersampled.

Data availability

The aligned laminography projections generated during the current study are available under the Creative Common license in the Zenodo repository, https://doi.org/10.5281/zenodo.2657340.

Received: 12 April 2019; Accepted: 23 August 2019;
Published online: 7 October 2019

References

1. Behrens, T. E. J. & Sporns, O. Human connectomics. *Curr. Opin. Neurobiol.* **22**, 144–153 (2012).
2. Shahmoradian, S. et al. Three-dimensional imaging of biological tissue by cryo X-ray ptychography. *Sci. Rep.* **7**, 6291 (2017).
3. Servanton, G. et al. Advanced TEM characterization for the development of 28-14 nm nodes based on fully-depleted silicon-on-insulator technology. *J. Phys.Conf. Ser.* **471**, 01202 (2013).
4. Gignac, L. M. et al. High energy BSE/SE/STEM imaging of 8 um thick semiconductor interconnects. *Microsc. Microanal.* **20**(S3), 8–9 (2014).
5. Holler, M. et al. High-resolution non-destructive three-dimensional imaging of integrated circuits. *Nature* **543**, 402 (2017).
6. Orji, N. G. et al. Metrology for the next generation of semiconductor devices. *Nat. Electron.* **1**, 532–547 (2018).
7. Robertson, J. & Riley, M. The big hack: how China used a tiny chip to infiltrate U.S. companies. *Bloomberg Businessweek* https://www.bloomberg.com/2018-the-big-hack (2018).
8. Pfeiffer, F. X-ray ptychography. *Nat. Photonics* **12**, 9–17 (2018).
9. Hasenkamp, F. A. Radiographic laminography. *Mater. Eval.* **32**, 169 (1974).
10. Helfen, L. et al. High-resolution three-dimensional imaging of flat objects by synchrotron-radiation computed laminography. *Appl. Phys. Lett.* **86**, 071915 (2005).
11. Helfen, L. et al. Synchrotron-radiation computed laminography for high-resolution three-dimensional imaging of flat devices. *Phys. Status Solidi A* **204**, 2760–2765 (2007).
12. Xu, F. et al. Correlative nanoscale 3D imaging of structure and composition in extended objects. *PLoS ONE* **7**, 6 (2012).
13. Holler, M. & Raabe, J. Error motion compensating tracking interferometer for the position measurement of objects with rotational degree of freedom. *Opt. Eng.* **54**, 054101 (2015).
14. Holler, M. et al. An instrument for 3D x-ray nanoimaging. *Rev. Sci. Instrum.* **83**, 073703 (2012).
15. Holler, M. et al. OMNY—a tOMography nano crYo stage. *Rev. Sci. Instrum.* **89**, 043706 (2018).
16. Myagotin, A. et al. Efficient volume reconstruction for parallel-beam computed laminography by filtered backprojection on multi-core clusters. *IEEE Trans. Image Process.* **22**, 5348–5361 (2013).
17. Kak, A. C., Slaney, M. & Wang, G. Principles of computerized tomographic imaging. *Med. Phys.* **29**, 107–107 (2002).
18. Chambolle, A. An algorithm for total variation minimization and applications. *J. Math. Imaging Vis.* **20**, 89–97 (2004).
19. van Heel, M. & Schatz, M. Fourier shell correlation threshold criteria. *J. Struct. Biol.* **151**, 250–262 (2005).
20. Stockmar, M. et al. Near-field ptychography: phase retrieval for inline holography using a structured illumination. *Sci. Rep.* **3**, 1927 (2013).
21. Tsai, E. H. R. et al. X-ray ptychography with extended depth of field. *Opt. Express* **24**, 29089–29108 (2016).
22. Eriksson, M. et al. Some small-emittance light-source lattices with multi-bend achromats. *Nucl. Instrum. Methods Phys. Res. A* **587**, 221–226 (2008).
23. Bilderback, D. H. et al. Design of doubly focusing, tunable (5-30 keV), wide bandpass optics made from layered synthetic microstructures. *Nucl. Instrum. Methods Phys. Res.* **208**, 251–261 (1983).
24. Kirkpatrick, P. & Baez, A. V. Formation of optical images by X-rays. *J. Opt. Soc. Am.* **38**, 766–774 (1948).
25. Howells, M. R. et al. An assessment of the resolution limitation due to radiation-damage in X-ray diffraction microscopy. *J. Electron Spectrosc. Relat. Phenom.* **170**, 4–12 (2009).
26. Odstrcil, M. et al. Fast positioning for X-ray scanning microscopy by a combined motion of sample and beam-defining optics. *J. Synchrotron Radiat.* **26**(Pt 2), 504–509 (2019).
27. Suzuki, A. et al. High-resolution multislice x-ray ptychography of extended thick objects. *Phys. Rev. Lett.* **112**, 053903 (2014).
28. Li, P. & Maiden, A. Multi-slice ptychographic tomography. *Sci. Rep.* **8**, 2049 (2018).
29. Odstrcil, M. et al. Ab initio nonrigid x-ray nanotomography. *Nat. Commun.* **10**, 2600 (2019).
30. Gorelick, S., Guzenko, V. A., Vila-Comamala, J. & David, C. Direct e-beam writing of dense and high aspect ratio nanostructures in thick layers of PMMA for electroplating. *Nanotech* **21**, 295303 (2010).
31. Holler, M. et al. X-ray ptychographic computed tomography at 16 nm isotropic 3D resolution. *Sci. Rep.* **4**, 3857 (2014).
32. Henrich, B. et al. PILATUS: a single photon counting pixel detector for x-ray applications. *Nucl. Instrum. Methods Phys. Res. A* **607**, 247–249 (2009).
33. Huang, X. J. et al. Optimization of overlap uniformness for ptychography. *Opt. Express* **22**, 12634–12644 (2014).
34. Thibault, P. et al. High-resolution scanning x-ray diffraction microscopy. *Science* **321**, 379–382 (2008).
35. Thibault, P. & Guizar-Sicairos, M. Maximum-likelihood refinement for coherent diffractive imaging. *New J. Phys.* **14**, 063004 (2012).
36. Guizar-Sicairos, M. et al. Phase tomography from x-ray coherent diffractive imaging projections. *Opt. Express* **19**, 21345–21357 (2011).
37. Guizar-Sicairos, M. et al. Quantitative interior x-ray nanotomography by a hybrid imaging technique. *Optica* **2**, 259–266 (2015).

38. Guizar-Sicairos, M. et al. High-throughput ptychography using Eiger: scanning x-ray nanoimaging of extended regions. *Opt. Express* **22**, 14859–14870 (2014).
39. Helfen, L. et al. On the implementation of computed laminography using synchrotron radiation. *Rev. Sci. Instrum.* **82**, 063702 (2011).
40. Harasse, S., Yashiro, W. & Momose, A. Iterative reconstruction in x-ray computed laminography from differential phase measurements. *Opt. Express* **19**, 16560–16573 (2011).
41. Crowther, R. A., DeRosier, D. J. & Klug, A. The reconstruction of a three-dimensional structure from projections and its application to electron microscopy. *Proc. R. Soc. Lond. A* **317**, 319 (1970).

Acknowledgements

The measurements were performed at the cSAXS beamline of the Swiss Light Source at the Paul Scherrer Institut.

Author contributions

Sample preparation was carried out by E.M., S.F. and A.F.J.L. The X-ray measurements were made by M.H., M.O. and M.G.-S. The PyXL endstation was developed by M.H. and J.R. The X-ray data were analysed and visualized by M.H., M.O. and M.G.-S. Specialized algorithms for alignment and processing of projections and laminography reconstruction were developed by M.O. The X-ray illumination lens was produced by M.L. and C.D. The X-ray detector was developed by G.T. The focused ion beam/SEM data were collected by J.Z., W.U. and A.F.J.L. The manuscript was written by M.H., M.O., M.G.-S., O.B., A.F.J.L. and G.A.

Competing interests

The authors declare no competing interests.

Additional information

Supplementary information is available for this paper at https://doi.org/10.1038/s41928-019-0309-z.

Correspondence and requests for materials should be addressed to M.H.